MagmaFOAM-1.0: a modular framework for the simulation of magmatic systems

Federico Brogi[1,2], Simone Colucci[1], Jacopo Matrone[3], Chiara P. Montagna[1], Mattia De' Michieli Vitturi[1,4], and Paolo Papale[1]

[1]Istituto Nazionale di Geofisica e Vulcanologia, sezione di Pisa
[2]Istituto Nazionale di Oceanografia e di Geofisica Sperimentale
[3]Dipartimento di Matematica, Università degli Studi di Firenze
[4]University at Buffalo, Department of Geology

Correspondence: F. Brogi (federico.brogi@ingv.it)

Abstract. Numerical simulations of volcanic processes play a fundamental role in understanding the dynamics of magma storage, ascent and eruption. The recent extraordinary progress in computer performance and improvements in numerical modeling techniques allow simulating multiphase systems in mechanical and thermodynamical disequilibrium. Nonetheless, the growing complexity of these simulations requires the development of flexible computational tools that can easily switch between sub-

5   models and solution techniques. In this work we present MagmaFOAM, a library based on the open source computational fluid dynamics software OpenFOAM, that incorporates models for solving the dynamics of multiphase, multicomponent magmatic systems. Retaining the modular structure of OpenFOAM, MagmaFOAM allows run-time selection of the solution technique depending on the physics of the specific process, and sets a solid framework for in-house and community model development, testing and comparison. MagmaFOAM models thermo-mechanical non-equilibrium phase coupling and phase change,

10   and implements state-of-the-art multiple volatile saturation models and constitutive equations with composition-dependent and space-time local computation of thermodynamic and transport properties. Code testing is performed using different multiphase modeling approches for processes relevant to magmatic systems: Rayleigh-Taylor instability, for buyoancy-driven magmatic processes; multiphase shock tube simulations, propedeutical to conduit dynamics studies; bubble growth and breakage in basaltic melts. Benchmark simulations illustrate the capabilities and potential of MagmaFOAM to account for the variety of

15   non-linear physical and thermodynamical processes characterizing the dynamics of volcanic systems.

1 Introduction

Simulating transport processes in volcanic systems is of crucial importance to understand the physics of eruptions, correctly interpret geophysical signals recorded by volcano monitoring systems, anticipate volcanic scenarios, and forecast volcanic hazards (Sparks, 2003; Bagagli et al., 2017). A great number of flow models have been developed to address specific volcanic

20   processes, including magma chamber dynamics (Ruprecht et al., 2008; Bergantz et al., 2015; Garg et al., 2019), conduit flow (Melnik, 2000; Papale, 2001; de' Michieli Vitturi et al., 2008b; Colucci et al., 2017b), volcanic plumes (Suzuki et al., 2005; Cerminara et al., 2016), pyroclastic flows (Esposti Ongaro et al., 2007; de' Michieli Vitturi et al., 2015; Dufek, 2016) and

lava flows (Griffiths, 2000). Inter-model comparison studies have evaluated individual model performance and the relevance of the different subprocesses, and have highlighted target areas for improvement (Massol and Koyaguchi, 2005; Macedonio

25   et al., 2005; Sahagian and Proussevitch, 2005; Costa et al., 2016). All these models attempt to tackle the great complexity arising from the presence of multiple phases. Interactions among liquid phases (e.g. silicate melt), solid phases (e.g. crystals or pyroclasts) and gas phases (exsolved volatiles or atmospheric gas) are indeed ubiquitous in volcanic systems, from deep magma chambers up into the atmosphere (e.g., Jackson et al., 2018; Keller and Suckale, 2019).

Volcanic transport processes are typically characterized by a wide range of spatial and temporal scales at which different

30   interacting physical subprocesses occur (Griffiths, 2000; Gonnermann and Manga, 2007; Dufek, 2016). From a modeling perspective, there is no general approach able to treat all these subprocesses at the same time, thus specific models are usually developed for each application.

A generic multiphase system can be thought of as composed by sub-domains or regions pertaining to single phases, separated by interfaces (boundaries) representing sharp discontinuities where the physical properties change abruptly. The typical size

35   of the interfaces can be comparable to, or orders of magnitude smaller than the domain and flow length scales; or even cover a broad range of scales. From a numerical point of view, depending on the spatial scale of the interfaces different solution strategies are required. Modeling efforts have therefore focused on developing regime-dependent strategies that attempt to adapt to the specifics of the flow to be resolved (e.g. Ishi and Hibiki, 2006). Interface-resolving methods, similar to direct numerical simulation (DNS) approaches in single-phase turbulent flows (Moin and Mahesh, 1998), fully resolve the scales

40   of the fluid equations and track the topology of the interfaces. These methods are practical only when the smallest scale of the flow and of the discontinuities are sufficiently large with respect to the grid size, and not too small with respect to the computational domain (Ishi and Hibiki, 2006). As a result, this approach has been used for instance to study large gas bubbles ascending in a conduit through low viscosity melts (Suckale et al., 2010a); bubble growth, deformation and coalescence (Huber et al., 2014); buoyancy-driven instabilities among liquids at different densities (Suckale et al., 2010b); and for the mush

45   microphysics characterizing crystal-rich magma reservoirs (Parmigiani et al., 2014). However, multiphase flows in nature often present dispersed interfaces (e.g. for bubbly, droplet or particle-laden flows), for which interface-resolving approaches are computationally too expensive. In this case, average forms of the flow equations can be adopted and the need of tracking the exact position of the interface is avoided. The phases are described as interpenetrating continua governed by separate sets of conservation equations. The so-called multi-fluid Eulerian approach is quite general and allows modeling thermo-mechanical

50   disequilibrium (e.g. phases with different velocities, temperatures or pressures) as well as interactions of the dispersed phases for any multi-phase system (Marchisio and Fox, 2007), including magmas (Keller and Suckale, 2019). Applications of multi-fluid modeling in volcanology include but are not limited to the study of buoyancy-driven magma mixing (Ruprecht et al., 2008), conduit dynamics (Papale, 2001; Dufek and Bergantz, 2005) and volcanic plumes (Neri et al., 2003; Ongaro et al., 2007). However, the solution of these models requires the use of additional system-dependent constitutive equations, valid for

55   specific flow regimes and/or concentrations of the dispersed phase. In addition, when dispersed phase relaxation times are small (e.g. for small particles and/or high fluid viscosities), the stability of the numerical solution requires a much smaller time step than the flow time scale, hence dramatically increasing the computational cost. Under the assumptions of thermo-mechanical

equilibrium, the equations of the multi-fluid model can be further reduced to the evolution equation of a single pseudo-fluid representing a mixture of multiple phases. Given the reduced number of equations needed to track the evolution of the mixture, this is a more convenient approach when there is a strong thermo-mechanical coupling between phases. Simulations of magma mixing (Longo et al., 2012; Garg et al., 2019) and conduit dynamics (de' Michieli Vitturi et al., 2008a; Melnik and Sparks, 2006) as well as volcanic plumes (e.g., Suzuki et al., 2005) are only few examples of application.

The increased ability of models to include detailed physics strictly requires the development of more flexible computational tools that can easily switch between constitutive models and solution techniques to adapt to different dynamical regimes, thereby reducing computational efforts, increasing usability and easily allowing scientists to perform inter-model comparison studies and models coupling.

The open source library OpenFOAM provides a variety of fluid solvers for multiphase flows, that can be combined with several different constitutive equations. Its modular object-oriented implementation allows the developers to easily expand and adapt the code, and the users to combine different models at run-time with almost no need to code. Given a set of discretised fluid evolution equations (or 'solver'), the user can easily select appropriate thermophysical and rheological models or switch from 2D/3D to axis/plane symmetric simulations. The OpenFOAM community is continuosly growing, as is the range of applications of interest for both the academy and industry (e.g., Winden, 2021). Moreover, the recently established exaFoam consortium will improve computational performance enabling the "OpenFOAM community to exploit efficently the current evolving HPC hardware and middleware" (www.exafoam.eu). OpenFOAM is thus an ideal platform for developing a computational toolbox for the next generation of magmatic systems modeling. In this work we present the MagmaFOAM library, an extension of OpenFOAM dedicated to solving multiphase volcanic flows. The current implementation features multiple volatile saturation models (Papale et al., 2006) and specific formulations for the equation of state (Lange and Carmichael, 1987) and viscosity (Giordano et al., 2008) of magmatic mixtures including dissolved volatiles. MagmaFOAM retains the basic coding principles of OpenFOAM, inherits its flexibility and takes full advantage of the family of fluid solvers and constitutive models (e.g. non-Newtonian rheological models) already implemented in OpenFOAM.

This paper is structured as follows. First we provide an overview of the basic ingredients of MagmaFOAM, including the specific magmatic constitutive equations and how they are implemented. Then, we show benchmarks and validation tests aimed at verifying the code ability to solve problems for segregated and dispersed flows of interest for magmatic systems with different modeling approaches. Finally, we summarize and discuss our results and draw the conclusions.

2 MagmaFOAM ingredients

2.1 Structure of MagmaFOAM

MagmaFOAM uses the same organization of OpenFOAM (Figure 1) and its hierarchy is therefore subdivided into applications and libraries (`src`). Code organization is therefore rational and efficient, reducing code duplication, promoting code reusage and facilitating testing. Most of the applications are assembled at run-time based on the user requests using dynamic linking to pre-compiled libraries: before running a simulation the user can arbitrarily select boundary conditions, discretization schemes,
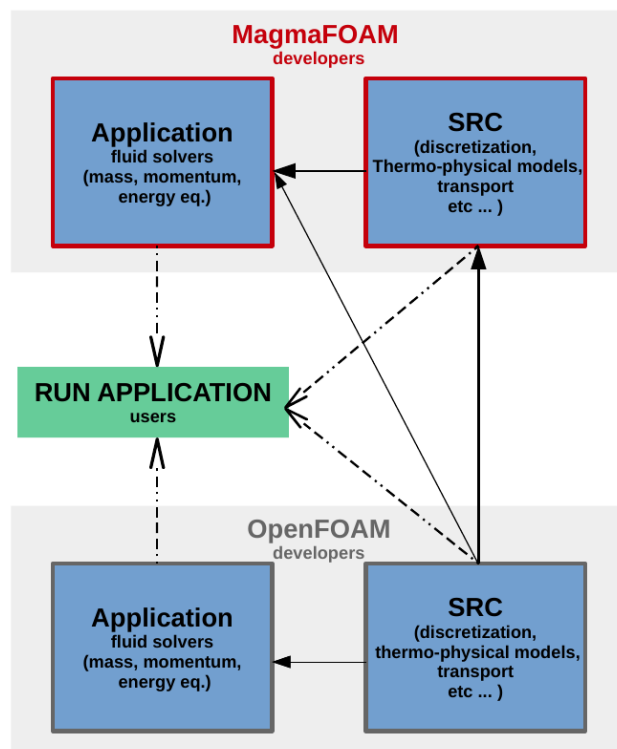
Figure 1. MagmaFOAM - OpenFOAM coupling scheme.

mixture and phase constitutive equations. This mechanism allows selecting and combining modeling ingredients, among the possible combinations, from both OpenFOAM and MagmaFOAM (Figure 1), without the need of coding.

2.1.1   Multi-component constitutive models for magmatic systems

The dynamics of magmas as they ascend, stall through the crust and possibly erupt is strongly dependent on their physical

95   properties (mostly density ρ and viscosity μ), which in turn are determined by composition and phase distribution, pressure p and temperature T conditions. The interplay among p-T conditions, melt-crystals-bubbles phase changes and density and viscosity variations originates a wealth of possible space and time patterns for magma storage, transport and eruption (e.g., Lesher and Spera, 2015). To handle this thermo-physical complexity, state-of-the-art multi-component constitutive models that compute melt properties as a function of the local pressure, temperature and composition have been implemented in

100   MagmaFOAM.

Multi-component volatile saturation is included through the SOLWCAD model (Papale et al., 2006), which provides equilibrium H_2O-CO_2 saturation over a broad range of $p-T$ conditions and for virtually any melt composition. This model overcomes the ideal Henrian behaviour, which is a reasonable approximation only at low pressures ($\lesssim 100\,\mathrm{MPa}$; Papale et al.,

2006). Once the phase distribution of volatile species is computed through SOLWCAD, the relevant physical properties for the
105   multiphase magma con be derived.

The density of the silicate melt up to a few GPa ($\lesssim 3\,\mathrm{GPa}$ or $\lesssim 100\,\mathrm{km}$ depth) is computed as in Lange and Carmichael
(1987) with an empirical equation of state, as a ratio of the oxides' molar masses (M_i) and molar volumes (V_i):

$$\rho(p,T,X) = \frac{M(X)}{V(p,T,X)} = \frac{\sum_i X_i M_i}{\sum_i X_i V_i(p,T)}, \tag{1}$$

where X_i is the mole fraction of the i-th oxide component. To a good approximation, molar volumes do not depend on melt
110   composition (Lesher and Spera, 2015) and can be computed with a polynomial expansion:

$$V_i(p,T) = \sum_{l,m} a^i_{l,m} T^l p^m = a^i_{0,0} + a^i_{1,0} T + a^i_{0,1} p + a^i_{1,1} pT + ... \tag{2}$$

The polynomial coefficients $a^i_{l,m}$ have been determined from laboratory experiments. For the oxides we have used the
coefficients reported by Lange and Carmichael (1987) and Lesher and Spera (2015). For H_2O and CO_2 we referred to Burnham
and Davis (1974) and Papale (1999), respectively.

115   Melt viscosity is described as in Giordano et al. (2008). This model includes temperature and compositional effects for a
wide range of melt compositions. In addition, the model can be used to determine the compositional dependence of important
viscosity-derived properties, such as melt glass transition temperature and fragility. This aspect may be particularly relevant
when modeling the ascent of degassing magma to determine the potential for brittle fragmentation. A drawback is that the
model does not take into account the effect of pressure on viscosity, which can become relevant when modeling magma
120   transport in the deep crust and mantle.

The model is based on the Tammann-Vogel-Fulcher (TFV) relationship for the non-Arrhenian temperature dependence of
the bubble-crystal free viscosity η:

$$\log \eta = A + \frac{B}{T - C}, \tag{3}$$

where T [K] is the temperature, A is a constant and B and C are parameters that depend on the melt composition, including
125   dissolved volatile species. The A constant provides a high temperature limit for viscosity ($\sim 10^{-4}\,\mathrm{Pa\,s}$), that holds for all
melts regardless of their composition and is supported by both theoretical considerations and experimental observations (e.g.
Scopigno et al., 2003).

2.2   Modeling volatiles concentration at the bubble-melt interface

Models accounting for multicomponent phase change require a description of the evolution of the composition at the interface
130   between phases. Typically, in multi-fluid solvers (e.g. `reactingTwoPhaseEulerFoam`), bubble growth is modeled by

computing the diffusive flux ($\dot{m}_i$) of a volatile specie i at the bubble-liquid interface as

$$\dot{m}_i = \rho k_i D_i \left(\Delta Y_i \right) \tag{4}$$

where ρ is the liquid density, k_i is the mass transfer coefficient and D_i is the diffusion coefficient (Cussler, 2009). ΔY_i is the difference between the mass fraction of the specie in the phase (Y_i) and at the interface: ($Y_{\mathrm{f},i}$)

$$\Delta Y_i = Y_i - Y_{\mathrm{f},i}. \tag{5}$$

Under the assumption of local equilibrium, the mass fraction at the interface can be expressed as

$$Y_{\mathrm{f},i} = Y_{\mathrm{eq},i} \left(p, T_{\mathrm{f}}, X, X_{Vtot} \right), \tag{6}$$

where $Y_{\mathrm{eq},i}$ is the saturation concentration of a specific volatile specie (i.e. mass fraction at thermodynamic equilibrium). In general this is a non linear function of pressure (p), temperature at the interface,(T_{f}), melt composition (X) and total amount of volatiles of all species (X_{Vtot}). For magmas with H_2O and CO_2, Y_{eq} can be computed using SOLWCAD (Papale et al., 2006) or other dedicated models (e.g., Newman and Lowenstern, 2002; Burgisser et al., 2015). Direct coupling of any fluid solver with these models is usually too computationally expensive. Therefore, MagmaFOAM solvers can read the saturation surface from a pre-processed table. During the simulation, tabulate values are interpolated (multilinear interpolation) and used to compute $Y_{\mathrm{eq},i}$ in Equation (6).

2.3 MagmaFOAM constitutive models

Constitutive models implemented in MagmaFOAM can be selected and combined at run-time (no need of coding) with existing OpenFOAM solvers suitable for the specific problem under consideration (Figure 1). For example, the MagmaFOAM model for silicate melt density can be used with any compressible solver, either single- or multi-phase. This constitutive model is not compatible with incompressible solvers, that require density to be constant; however, in this case the density of the incompressible fluid can be preliminarily defined taking advantage of the dedicated MagmaFOAM utility `magmaThermoMixture`. The latter can also be used for testing implemented models as it simply returns the thermophysical properties as a function of composition, pressure and temperature. Demonstrative tutorials are included in MagmaFOAM to show how the end user can accomplish all these tasks at run-time using both single-phase and multiphase solvers.

2.4 Models for multicomponent bubble growth

Volatiles' phase changes and bubble growth are ubiquitous processes in volcano dynamics (Proussevitch and Sahagian, 1998). The gas exsolution process begins with the nucleation of bubbles in an oversaturated melt and continues with bubble growth. Bubbles grow by mass diffusion, when the silicate melt is oversaturated in volatiles, and by mechanical expansion as a response to pressure decrease. The viscosity of the surrounding melt and the surface tension oppose a resistance to bubble growth and control the mechanical disequilibrium between the bubbles and the melt itself. A number of works (Proussevitch et al., 1993;

Lyakhovsky et al., 1996; Proussevitch and Sahagian, 1998; Lensky et al., 2001, 2004; Chouet et al., 2006; Shimomura et al., 2006; Coumans et al., 2020) solve the system of bubbles as a monodisperse periodic array of static, spherical, single-component (H_2O) growing bubbles surrounded by a viscous melt shell, using the Rayleigh-Plesset equation. A suite of models, based on a similar approach, have been implemented in MagmaFOAM and benchmarked to simulate multicomponent diffusive bubble growth. This approach, despite the strong assumption that the size distribution remains monodisperse at all times, provides an accurate representation of the coupled momentum balance and diffusive transport of volatiles, and represents a powerful tool for studying bubble growth in silicate melts (e.g., Coumans et al., 2020). This method is expected to produce accurate results especially at low vesicularity, since it accurately resolves the concentration profile near the bubble interface (Huber et al., 2014). All model equations can be found in Appendix B and are solved as a systems of ordinary differential equations (ODEs) using the OpenFOAM ODE solvers.

3 Benchmarks and test cases

The test cases presented here are included in the MagmaFOAM distribution together with the relevant post-processing routines. The results shown here are thus fully reproducible, and the benchmarks can be used to study the accuracy and efficiency of other OpenFOAM or external solvers.

3.1 Interface resolving modeling

The Volume of Fluid method (VOF) is adopted in OpenFOAM to resolve the position and shape of the interface separating two fluids or phases (e.g. liquid-gas). This methodology treats the interface discontinuity as a smooth but rapid variation (few computational cells) of an indicator field (volumetric fraction) representing the relative presence of one phase with respect to the other in each cell. The evolution of the interface is then obtained by simply advecting the volumetric fraction using the velocity field computed from a single (e.g. the OpenFOAM solver `interFoam`) or multi-fluid momentum equations (e.g. the OpenFOAM solver `multiphaseEulerFoam`). With respect to other methods, VOF is generally mass conservative but requires special techniques to avoid numerical diffusion of the interface during advection. Specifically, `interFoam` makes use of an additional compressive term in the advection equation that counter-balances the numerical blur of the interface (Deshpande et al., 2012). `interFoam` solves flows characterized by constant, or slowly-varying with respect to the flow time scales, fluid properties. Relevant volcanic scenarios are for example gas-poor magmatic reservoirs at depth, characterized by relatively fast overturn times (Ruprecht et al., 2008; Perugini et al., 2010; Montagna et al., 2015).

Here we present benchmarks and test cases to evaluate the accuracy of the solver `interFoam` to explore the dynamics of two immiscible fluids separated by a free interface. Specifically, we perform detailed studies of buoyancy-driven magma mixing and rising bubble dynamics. Overall, we find a remarkably good agreement between our simulation results and theoretical or numerical results from literature, over different flow regimes of interest for magma dynamics. The numerical solutions relative to cases with low Reynolds number Re are very accurate. At larger Re, the results are less accurate due to the appearence of high frequency numerical noise that can trigger secondary spurious interface instabilities. Reducing numerical noise by

adopting different numerical schemes is one relevant element for future investigation. The magnitude of the compressive term, used in the solver to prevent numerical smearing of the interface, is a free parameter in the simulations and may influence the accuracy of the solution depending on the problem parameters. More recent OpenFOAM versions include more rigorous and

195   accurate interface-resolving methods (e.g. Roenby et al., 2017).

3.1.1 Magma mixing

Magma mixing and mingling are widespread phenomena in volcanic plumbing systems (Perugini and Poli, 2012; Morgavi et al., 2017), and they have often been invoked as eruption triggers (Wark et al., 2007; Druitt et al., 2012; Martí et al., 2020). Magma mixing is typically driven either by gravitational Rayleigh-Taylor instabilities, involving contacts between magmas

200   with different densities due to compositional, thermal or phase stratifications (e.g., Jellinek et al., 1999; Montagna et al., 2015; Garg et al., 2019); or by percolation of pressurized magmas arriving from depth into mushy reservoirs (Bachmann and Bergantz, 2003; Seropian et al., 2018).

A standard benchmark to test numerical solvers for Rayleigh-Taylor instability problems requires to compare computed growth rates for small-amplitude single-mode perturbations with the linear stability theory. The latter predicts that a small

205   perturbation grows exponentially with a rate that depends on its wavelenght and on fluid density and viscosity contrasts (Chandrasekhar, 1955), surface tension (Chandrasekhar, 2013), compressibility (Mitchner and Landshoff, 1964) and diffusivity (Duff et al., 1962; Xie et al., 2017). The problem parameters can be expressed by two dimensionless numbers: the Atwood number $\mathrm{Atw} = (\rho_h - \rho_l)/(\rho_h + \rho_l)$ and the Reynolds number ($\mathrm{Re} = \sqrt{Wg}W/\nu$), where ρ_h and ρ_l are the two liquid densities, ν is the kinematic viscosity ($\nu_h = \nu_l$), W is the wavelength of the perturbation and g is the gravitational acceleration. We consider a

210   2D rectangular domain with a no-slip condition (walls) on top and bottom boundaries and periodic conditions on the sides. The interface between the two liquids is located at the center of the computational domain (Figure 3). The size L of the computational box is determined by the wavelength of the initial perturbation ($L = W \times 2W$). Benchmark results are reported in Figure 2 for Atwood numbers relevant for natural melts. The computed growth rates are in agreement with the theory (Xie et al., 2017) for different wavelengths (or equivalently wave numbers $k = 2\pi/W$) of the perturbation. The solver underestimates the

215   peak growth rates at low k, corresponding to high Re. A more in-depth analysis of the results (Appendix A) reveals that this discrepancy is mainly due to an initial delay in the onset of the perturbation. Removing this initial offset, the computed growth rates result much more accurate. Smaller initial perturbation amplitudes also improve accuracy.

As the instability grows and its amplitude becomes comparable with its wavelength, non-linear effects become dominant and the linear theory is not valid to predict the evolution of the system anymore. In order to validate `interFoam` for non-linear

220   regimes we have compared our results with He et al. (1999) for single-mode perturbation with a 10% amplitude-to-wavelength ratio, Atwood number $\mathrm{A} = 0.5$ and Reynolds number $\mathrm{Re} = 256$. A remarkably good agreement is obtained for the evolution of the fluid interface (Figure 3) using the same resolution (256 x 1024 cells). Convergence of the results was tested for different space and time resolutions using adaptive time-step based on maximum allowed Courant Number ($\mathrm{Co_{max}} = 0.5$) to speed up the simulation. For a given mesh resolution the accuracy and convergence of the solution depend on the values of $\mathrm{Co_{max}}$ and

225   number of iterations (`nIter`) used to solve the pressure-velocity coupling with the PISO algorithm (Issa, 1986). Generally,
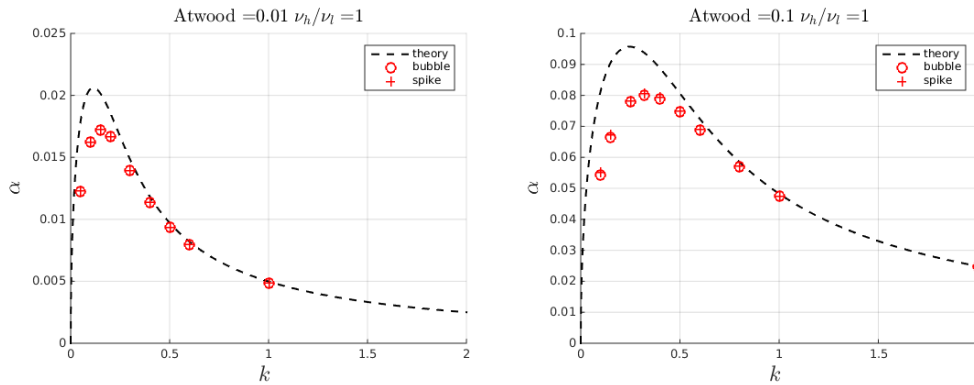
Figure 2. Comparison between computed growth rates (symbols) of the Rayleigh Taylor instability in the linear regime obtained with the solver `interFoam` and theoretical ones (dashed line). Bubble growth rates are computed tracking the position of the interface with respect to the central axis of the domain while spike growth rates are computed with respect to one of the lateral boundaries.
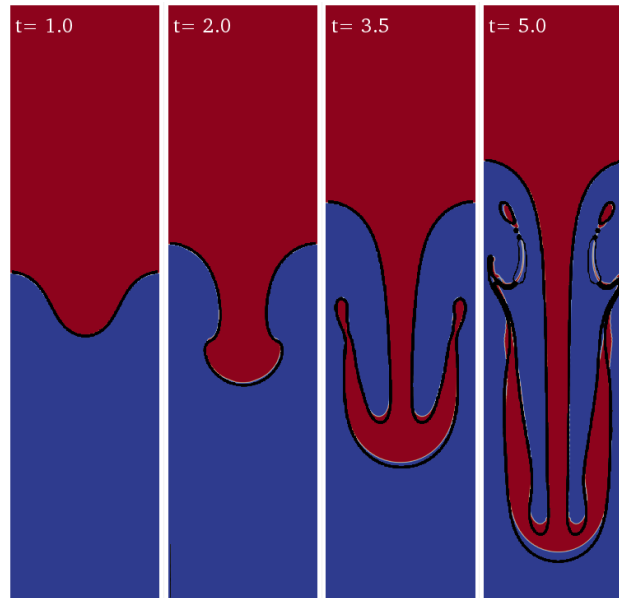
Figure 3. Rayleigh-Taylor instability ($A = 0.5, Re = 256$) computed with OpenFOAM solver `interFoam`. The density field (color-coded) is compared with the density countours in He et al. (1999) (black lines).

larger Co_{max} (< 1 for numerical stability) require larger `nIter` for solution convergence; our experience suggests that a relatively high number of `nIter` balances larger values for Co_{max}, reducing computational times. This way, even if the errors relative to the continuity equation are larger, the solution is not affected significantly.

(a)   (b)
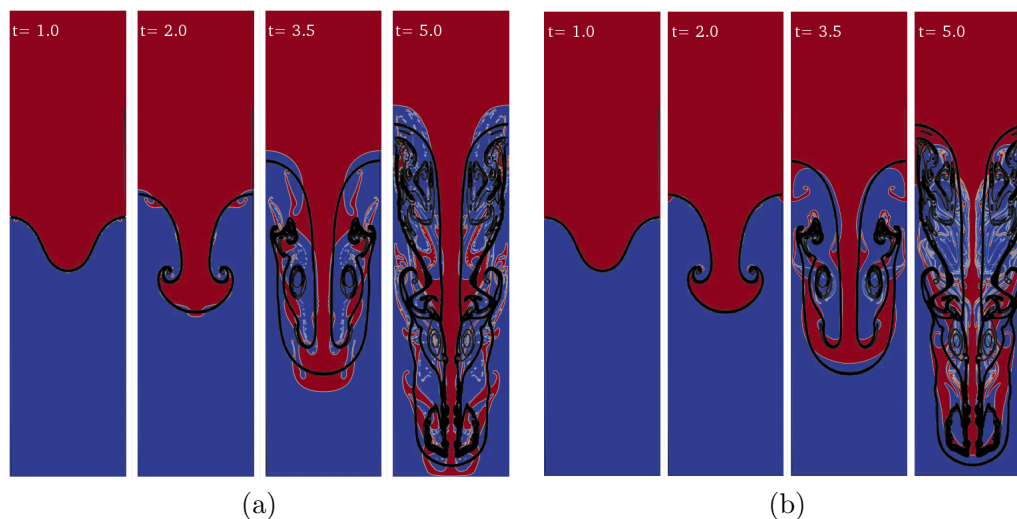
Figure 4. Rayleigh-Taylor instability ($A = 0.5, Re = 2048$) computed with OpenFOAM solver `interFoam` (in color) with: (a) 256×1024 cells and default value for interface compression factor $C_\alpha = 1$; (b) 512×2048 cells and $C_\alpha = 0.1$. The density field (color-coded) is compared with the density countours of He et al. (1999) (black lines).

For the high-Reynolds-number test case ($Re = 2048$) of He et al. (1999), the quality of the solution deteriorates using the
230   same resolution (Figure 4). The interface is deformed by artificial secondary instabilities most probably triggered by spurious numerical noise. Removing the interface compression term and doubling the number of cells improves the solution to nearly match the reference.

    We now explore gravity-driven mixing among two natural silicate melts (Figure 5). Density and viscosity of the two melts are computed a-priori using the MagmaFOAM utility `Test-magmaThermoMixture`. As a test case, we reproduce at small
235   scale a typical (Garg et al., 2019) interaction among a volatile-rich basalt ($X_{H_2O} = 2\,wt\%$) and a chemically more evolved andesitic melt. Temperature is set to $T = 1300\,^{\circ}C$ and pressure is atmospheric. Melt compositions are reported in Table D1. The relevant dimensionless numbers are now $A = 0.0167982$ and $Re = 54.065$ for a physical domain $1\,m$ x $4\,m$. Surface tension is again neglected. Compared to the previous simulations (e.g., Figure 3), the two liquids have now different kinematic viscosities. The larger viscosity ratio requires to increase significantly the numbers of iterations (≈ 300) needed to solve
240   pressure-velocity coupling (keeping $Co_{max} = 0.5$). As a result, the simulation is computationally much more demanding. The simulated time covers the entire overturning process (Figure 5).

3.1.2 Rising bubble dynamics

We consider a gas bubble rising in a basaltic melt. The bubble, initially at rest, rises due to buoyancy assuming a variety of shapes depending on the system parameters (e.g., liquid viscosity, surface tension, density contrast). Samkhaniani et al. (2012)
245   demonstrated the ability of `interFoam` to reproduce the different bubble shapes reported in the Grace diagram (Grace, 1973).
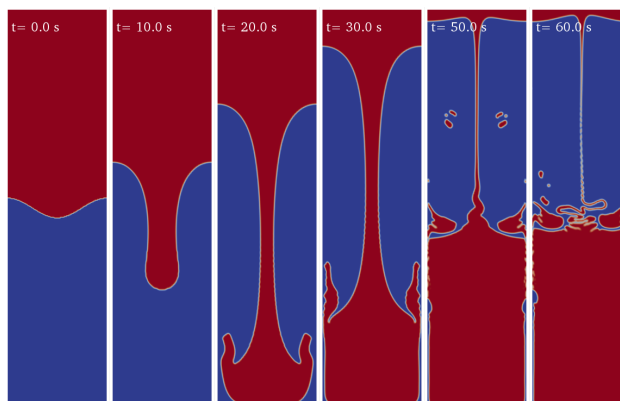
Figure 5. Rayleigh-Taylor instability between a volatile-rich ($X_{\mathrm{H_2O}} = 2\,\mathrm{wt\%}$) basalt (bottom) and andesite (top) computed with OpenFOAM solver `interFoam` (color-coded). The physical domain size is $1\,\mathrm{m} \times 4\,\mathrm{m}$.

Our contribution here focuses on the validation of the solver for bubble stability in magmas, through comparison with Suckale et al. (2010a) that used a different numerical method (Figure 6). In this set of 2D simulations, the main goal is to investigate the ability of the solver to reproduce the breakage of a bubble in relation with the shape that it may assume during its rise. Breakage may occur because of the small, random perturbations that form at the melt-bubble interface. No-slip boundary conditions are used for top and bottom boundaries and periodic conditions for the sides. In volcanic context, two parameters change significantly with respect to water experiments Samkhaniani et al. (2012): the density ρ and the viscosity μ of the liquid. While for water $\rho = 10^3\,\mathrm{kg/m^3}$ and $\mu = 10^{-3}\,\mathrm{Pa\,s}$, even a low-viscosity silicate melt (e.g., basalt) has viscosity values of order 10-100 Pa s and the density is above $2500\,\mathrm{kg/m^3}$. Surface tension is $\sigma = 0.073\,\mathrm{N/m}$ for water, while a reasonable value for magmas is $\sigma = 0.15\,\mathrm{N/m}$ (Colucci et al., 2016). In our tests we set $\sigma = 0.3\,\mathrm{N/m}$ and $\rho = 3500\,\mathrm{kg/m^3}$ to be consistent with Suckale et al. (2010a). With a being the bubble radius and v_0 the rise velocity, the relevant non-dimensional numbers derived directly from the governing equantions for an incompressible melt are (Suckale et al., 2010a): Reynolds number $\mathrm{Re} = \frac{\rho v_0 a}{\mu}$ (inertial to viscous forces), Froude number $\mathrm{Fr} = \frac{v_0^2}{ga}$ (inertia to buoyancy forces), Weber Number $\mathrm{We} = \frac{v_0^2}{ga}$ (inertia to surface tension) and liquid to gas viscosity ratio $\Pi = \mu/\mu_g$. We can also define the Eötvös number (Eo), which is a combination of Fr and We ($\mathrm{Eo} = \mathrm{Fr}^{-2}\mathrm{We}$). Considering a constant $\Pi = 10^{-6}$, bubble regimes can be classified using only two adimensional numbers, Re and Eo. The Reynolds number mainly controls bubble stability and breakup, which is predominant at high Re. The Eötvös number instead plays an important role in determining bubble deformation. Indicatively, for $\mathrm{Eo} < 1$ and $\mathrm{Re} < 1$ the bubble is stable and preserves its initial spherical shape even in the presence of small perturbations of its interface. For $\mathrm{Eo} > 1$ and $\mathrm{Re} < 1$ the bubble deforms and may breakup if random perturbations affect significantly its surface, while for $\mathrm{Eo} > 1$ and $\mathrm{Re} > 1$ breakup occurs invariably.

Overall, breakup mechanisms are well reproduced in our simulations and bubble shapes at given non-dimensional times are consistent with those reported by Suckale et al. (2010a) for similar values of the non-dimensional numbers (Figure 6) and similar space resolution (20 cells per bubble radius). For the no breakup regime (Figure 6a), the bubble shape in our simulation
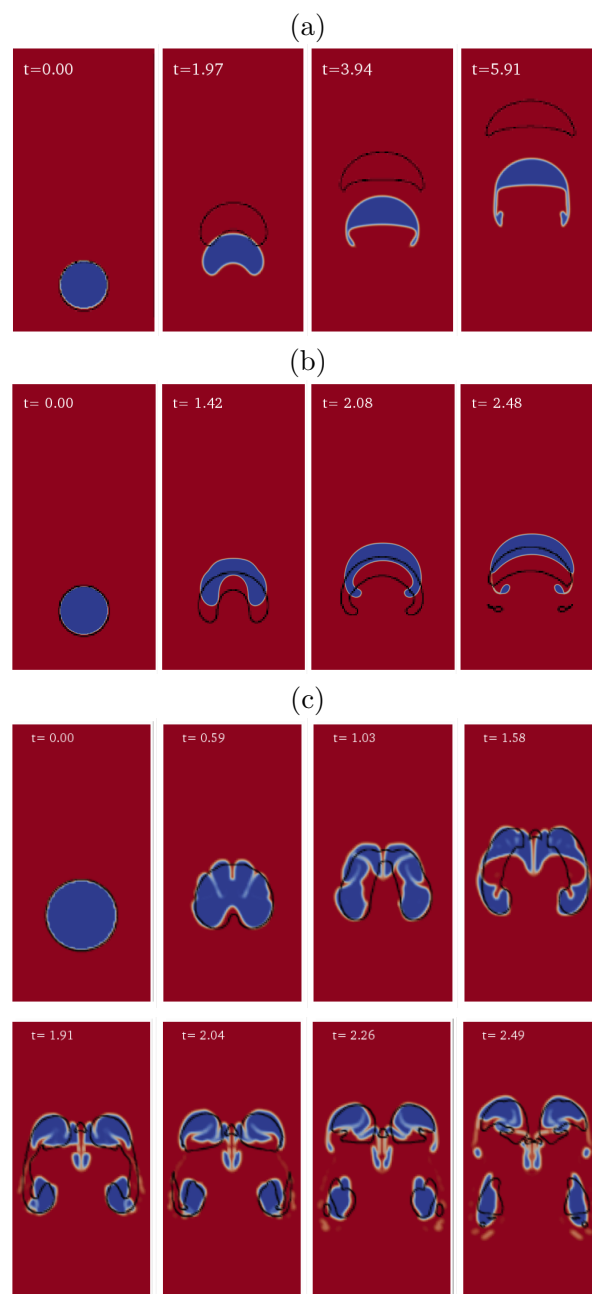
Figure 6. Simulation of bubble rise in a basaltic melt using `interFoam` are compared with the results of Suckale et al. (2010a) (black lines) for three different regimes: (a) No breakup ($Re \approx 5$, $Fr \approx 0.4$, $We \approx 90$, and $\Pi = 10^{-6}$), (b) Gradual breakup ($Re \approx 25$, $Fr \approx 0.3$; $We \approx 800$, and $\Pi = 10^{-6}$); (c) Catastrophic breakup ($Re \approx 250$, $Fr \approx 0.16$, $We \approx 1350$, and $\Pi = 10^{-6}$). For each regime, snapshots at different non-dimensional times are shown.
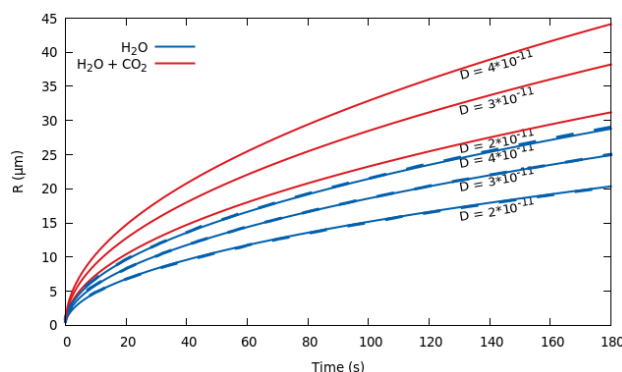
Figure 7. Temporal evolution of bubble radius. In blue the comparison between the solutions obtained with the MagmaFOAM model `multiComponentODERPShellDStatic` (solid lines) and the numerical solutions from Lyakhovsky et al. (1996) (dashed lines) under three different values of diffusion coefficient. Red lines represent the same simulations with 1% of CO_2 added. $\rho_l = 2300\,\mathrm{kg/m^3}$, $\mu = 5 \cdot 10^4\,\mathrm{Pa\,s}$, $\sigma = 0.06\,\mathrm{N/m}$, $T = 1123\,\mathrm{K}$, $p_0 = 150\,\mathrm{MPa}$, $\Delta p = 30\,\mathrm{MPa}$, $R_0 = 10^{-7}\,\mathrm{m}$, $S_0 = 2 \cdot 10^{-4}\,\mathrm{m}$, $C_0^{\mathrm{H_2O}} = 0.053$. The diffusion coefficient of CO_2 is one order of magnitude smaller.

displays two additional thin wings. In the gradual breakup regime (Figure 6b) small droplets are formed at the rear of the bubble. The results are reported here with higher resolution (40 cells per bubble radius), since with lower resolution the bubble

270 presents a slightly different shape with a flatter head. In the catastrophic breakup regime (Figure 6c), the bubble immediately collapses forming a large number of small to medium sized bubbles.

3.2 Diffusive bubble growth

Here we demonstrate the ability of the ODE solver `multiComponentODERPShellDStatic` to simulate bubble growth in a rhyolitic melt by expansion and mass diffusion.

275 Our solution has been benchmarked by comparison with Lyakhovsky et al. (1996) for the diffusive growth of water gas bubbles under instantaneous decompression of a hydrated rhyolitic melt. To reproduce the reference solution we assumed a quasi-static diffusion in the liquid shell around the bubble. The quasi-static approximation holds when diffusion is fast relative to decompression rate (Lensky et al., 2004). The reference solutions for three different values of the diffusion coefficient are well reproduced by our model (Figure 7). We repeat the same simulations with the addition of 1% of CO_2 (red lines in Figure 7).

280 The multicomponent saturation surface is calculated using SOLWCAD (Papale et al., 2006). The bubble radius increases by $\approx 50\%$ and the gas volume fraction triplicates (see Equation (B6)).

3.3 Eulerian multi-fluid modeling

In this section we test the ability of the OpenFOAM two-fluid eulerian solver `reactingTwoPhaseEulerFoam` to deal with flow problems with a large number of small (unresolved) gas bubbles dispersed into a liquid phase. `reactingTwoPhaseEulerFoam`,

285 coupled with the magmaFOAM libraries, is tested in problems involving multiphase shock tubes as well as by simulating a multiphase-multicomponent reacting box.

3.3.1 Shock Tube Simulations

Decompression of a pressurized bubbly magma is a common trigger of explosive volcanic eruptions (e.g., Gonnermann and Manga, 2007). When a high-pressure magma reservoir is decompressed, a shock wave and a contact wave propagate into

290 the low pressure region, typically the atmosphere, and a rarefaction wave propagates into the bubbly magma (Koyaguchi and Mitani, 2005; La Spina et al., 2017), akin to shock tube devices. The latter have been extensively used to study wave propagation phenomena in compressible fluids. Usually high and low pressure regions are separated by a diaphragm, the instantaneous removal of which initiates highly transient dynamics (Stadtke, 2006). Assuming strictly one-dimensional flow conditions (i.e., ignoring the effects of shear viscosity), the shock tube mathematically represents a Riemann problem where the initial velocities

295 on both sides have been set to zero. For the specific case of ideal equation of state, an analytical solution can be derived for a pure single phase (Stadtke, 2006). Multiphase flow processes are generally governed by deviations from mechanical and thermal equilibrium between the phases. Nevertheless, the assumptions of homogeneous flow (equal phase velocities) and thermal equilibrium between the phases allow us to define a special limiting case for which a semi-analytical solution can be derived (Stadtke, 2006). We test the `reactingTwoPhaseEulerFoam` solver in inviscid one-dimensional and viscid

300 axisymmetric simulations of single-phase and two-phase shock tubes. Axisymmetric simulations allow us to investigate the effect of melt viscosity on the radial velocity profile, through the Giordano et al. (2008) model. The Lange and Carmichael (1987) equation of state is tested here for the propagation of rarefaction and shock waves.

Single phase We perform a standard Sod shock tube benchmark for pure air gas using a perfect gas equation of state. A nearly perfect agreement between the simulation and the analytical solution has been found by discretizing the one-dimensional

305 computational domain with 5000 cells. Then, we test the solver by simulating a shock-tube with pure liquid water using the SPWAT equation of state (Stadtke, 2006) implemented in MagmaFOAM. Discretizing the computational domain with the same number of cells, the contact and shock wave discontinuities are well resolved and do not display any instabilities. Finally, we perform a shock-tube simulation with pure liquid basalt (Table D1) using the equation of state for silicate melts proposed by Lange and Carmichael (1987) and implemented in MagmaFOAM. We use the same computational domain and the same

310 numerical schemes used in the liquid water test. Across the shock discontinuity the solution is more diffusive compared to the test for liquid water, while the contact discontinuity is still well resolved. The Figures for the single phase shock tubes described above are reported in Appendix C.

Two-phase We perform two-phase shock tube simulations for gas air-liquid water and gas water-liquid basalt (Table D1) shock tubes (Figures 8, 9, 10). The equations of state for each phase are the same as for the single-phase cases. In all the

315 simulations, the size of the dispersed phase (i.e., gas bubbles or liquid droplets), instead of being determined by a proper model (i.e., bubble growth model), is kept constant and used as a tuning parameter. This unphysical assumption allows us to control the mechanical and thermal disequilibrium between the gas and liquid phases in order to compare the simulation with the

limiting analytical solution for a homogeneous flow (Stadtke, 2006). It is worth noting that, even if the size of the dispersed phase is kept constant, its volume fraction can change according to the mass conservation equations.

320   First, we benchmark the solver with a gas air-liquid water shock tube for which a limiting analytical solution is provided (Stadtke, 2006) (Figure 8). Initial gas volume fraction is 0.1 in the high-pressure region (to the left of the interface) and 0.05 in the low-pressure region (to the right of the interface). Overall, we find a remarkable good agreement with the exact solution. The contact and shock wave discontinuities are well resolved and do not display any instabilities. The numerical solution is only slightly diffusive at the onset of the rarefaction wave. The overshoot visible in the velocity is produced by the mechanical

325   decoupling between the liquid and the dispersed gas phase (Stadtke, 2006) and disappears reducing the bubble size, as will be discussed in the next subsection.

The same simulation setup is used to simulate basalt (liquid) - water (gas) shock tube (Figure 9). In this case the simulation is axisymmetric, in order to understand the role of melt viscosity. The shape of axial profiles of pressure, velocity, gas volume fraction and mixture density are similar to 1D shock tube (Figure 8) for the air-water system. Velocity profiles along radial

330   coordinate are flat with a narrow boundary layer near the walls. In this case the higher viscosity ($\approx 10\,\mathrm{Pa\,s}$) drastically reduces the mechanical phase decoupling and the phase velocities are superimposed.

Finally, we use the same simulation setup of Figures 8 and 9, but with an initial gas volume fraction in the low pressure region (to the right of the interface) equal to 1 (Figures 10 and C4 in Appendix C). This configuration is more appropriate for a volcanic application where the shock wave travels in the atmosphere. In this case the continuous and dispersed phases can

335   invert, thus the bubbly flow, where bubble are dispersed in the continuous liquid phase, becomes a particle flow, where the liquid droplets are dispersed in the gas. This process, usually called fragmentation in volcanological literature, can be modelled, as a first approximation, using a critical volume fraction criterion ($0.5 < \alpha < 0.7$; e.g., La Spina et al., 2017). When the rarefaction wave propagates into the high pressure region (i.e., left side), the bubbly magma expands, accelerates and fragments. Due to the higher compressibility of the gas phase compared to the liquid melt, the temperature subplot shows phase decoupling during

340   expansion, the amount of which depends on the adopted heat transfer model.

The phase coupling problem Even if we limit to bubbly flow regimes, magmatic system are characterized by a wide range of viscosities (from $0.1\,\mathrm{Pa\,s}$ to $10^9\,\mathrm{Pa\,s}$) and bubble sizes (from few microns to decimeters). The bubble relaxation time (τ_b) is directly proportional to the square of the bubble diameter and inversely proportional to the kinematic viscosity of the continuous liquid phase ($\tau_b \propto D_b^2/\nu_l$). In magmatic phenomena, when considering small bubbles (e.g., $100\,\mu\mathrm{m}$) and even relatively low

345   viscosities (e.g., $10\,\mathrm{Pa\,s}$), τ_b can reach very small values ($\tau_b \approx 10^{-6}\,\mathrm{s}$), resulting in very strong mechanical phase coupling. Numerical algorithms like the one implemented in OpenFOAM, based on segregated solvers, require special care in order to ensure convergence of the solution when phase coupling is tight (Karema and Lo, 1999). The Partial Elimination Algorithm (PEA), implemented in OpenFOAM, shows the best convergence performance compared to other algorithms (Karema and Lo, 1999; Venier et al., 2016). Here we test the PEA method for shock tube simulations conditions within the range of interest

350   for magmatic applications. In Figure 11 we compare the analytical solution to the simulation results for different values of τ_b obtained by changing the bubble diameter. Decreasing τ_b from $10^{-1}\,\mathrm{s}$ to $10^{-3}\,\mathrm{s}$ the velocities of the two phases tend to overlap as expected, and agree with the homogeneous analytical solution. However, by further decreasing τ_b the solution diverges even
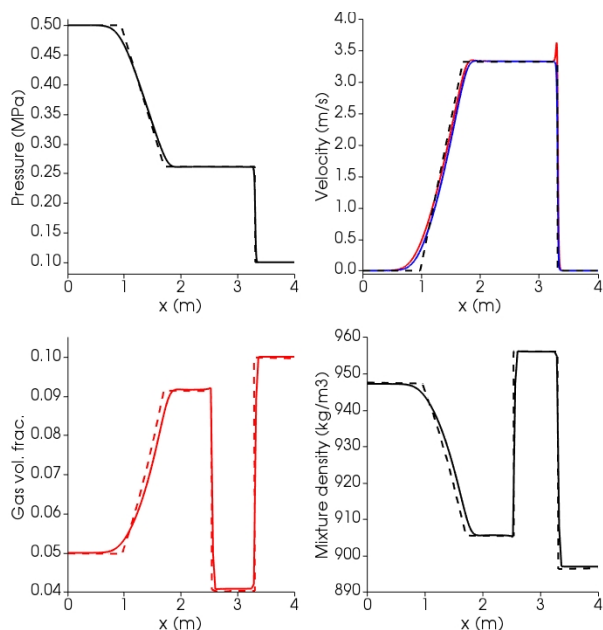
Figure 8. Results at time $t = 0.015\,\mathrm{s}$ for the air-water shock tube using the SPWAT EOS. Solid lines: OpenFOAM; dashed lines: analytical solution (Stadtke, 2006); Black lines: mixture; Blue lines: liquid (water); Red lines: gas (air). Mixture density is calculated a posteriori as $\rho_{\mathrm{mix}} = \alpha_{\mathrm{g}}\rho_{\mathrm{g}} + (1 - \alpha_{\mathrm{g}})\rho_{\mathrm{l}}$, where l is liquid and g is gas. At time 0, the interface dividing high pressure (left, l) from low pressure (right, r) zone is placed at 2.5 m. Initial conditions: $P_{\mathrm{l}} = 0.5\,\mathrm{MPa}$, $P_{\mathrm{r}} = 0.1\,\mathrm{MPa}$; $T_{\mathrm{l}} = T_r = 300\,\mathrm{K}$ for both phases; gas volume fraction $\alpha_{\mathrm{l}} = 0.05$, $\alpha_{\mathrm{r}} = 0.1$; $U_{\mathrm{l}} = U_{\mathrm{r}} = 0$ for both phases. Isobaric heat capacities of gas air and liquid water are, respectively, $Cp_{\mathrm{g}} = 1004.5\,\mathrm{Jkg^{-1}K^{-1}}$ and $Cp_{\mathrm{l}} = 4195\,\mathrm{Jkg^{-1}K^{-1}}$ (https://webbook.nist.gov/). Prandtl numbers of air and water are, respectively, 0.7 and 2.289, corresponding to thermal conductivities of $0.02\,\mathrm{W\,K^{-1}m^{-1}}$ and $0.67\,\mathrm{W\,K^{-1}m^{-1}}$ (https://webbook.nist.gov/).

when increasing 40 times the number of corrector cycles. This is an important limitation in the use of the multi-fluid solver. A possible workaround, currently under investigation, is to implement a limiter for the relaxation time.

355 3.3.2 Reacting box

A many-bubble system at zero gravity where bubbles grow by mass diffusion is analyzed here. The liquid phase is a basaltic melt (Table D1) with dissolved water and carbon dioxide whose properties are modelled by the Lange and Carmichael (1987) equation of state and the rheological equation of Giordano et al. (2008). The ideal gas equation of state has been used for the gas phase. As this is a many-bubble system, bubble growth is approximated through a subgrid model (see section 2.2). The

360 mass transfer coefficient (i.e., k_i in Equation (4)) is calculated according to a spherical model and the heat transfer coefficient according to spherical and Ranz-Marshall models, both already implemented in OpenFOAM. In addition, the I group IATE model (Ishi and Hibiki, 2006) is used to compute the surface area required by mass and heat transfer coefficient. The Interfacial
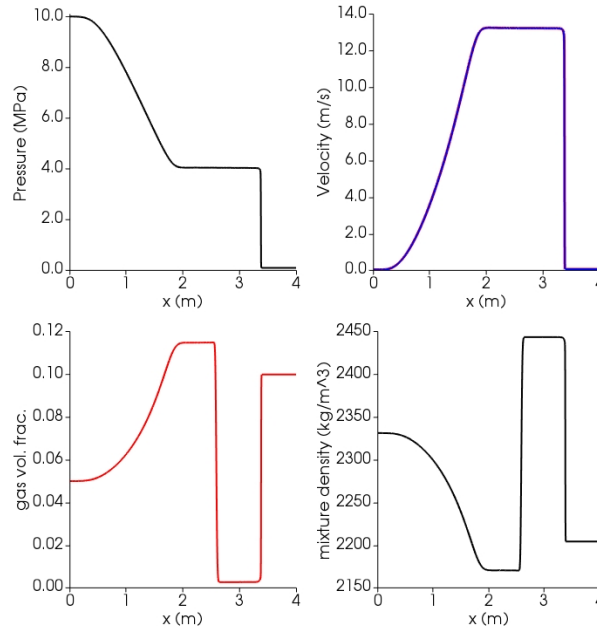
Figure 9. Results at time $t = 0.0065$ s for the axisymmetric gas water-basalt shock tube using the Lange-Carmichael EOS (Lange and Carmichael, 1987) and the viscosity model of Giordano et al. (2008). Blue lines: liquid (basalt); Red lines: gas (water). At time 0, the interface dividing high pressure (left, l) from low pressure (right, r) zone is placed at 2.5 m. Initial conditions: $P_l = 10$ MPa, $P_r = 0.1$ MPa; $T_l = T_r = 1273$ K for both phases; gas volume fraction $\alpha_l = 0.05$, $\alpha_r = 0.1$; $U_l = U_r = 0$ for both phases. Isobaric specific heat capacities in the gas and liquid phase are, respectively, $C_{P_g} = 2510$ J/kg^{-1}K^{-1} (https://webbook.nist.gov/) and $C_{P_{l,H_2O}} = 2278$ J/kg^{-1}K^{-1}, $C_{P_{l,basalt}} = 1600$ J/kg^{-1}K^{-1} (Lesher and Spera, 2015). Thermal conductivity of the liquid is 1.5 W K^{-1}m^{-1} (Lesher and Spera, 2015); for the water gas phase a Prandtl number of 0.9 is used, corresponding to a thermal conductivity of 0.14 W K^{-1}m^{-1} (https://webbook.nist.gov/)

.

Area Transport Equation (i.e., IATE) is a fundamental equation, formulated from the Boltzmann transport equation, describing the change of surface area between phases, assuming spherical shape of the dispersed phase (Ishi and Hibiki, 2006).

365   At time zero, a small amount of gas is uniformly distributed in the box and the liquid-gas system is out of thermodynamic equilibrium because the liquid is oversaturated in both H_2O and CO_2. After $\approx 4 \cdot 10^5$ s, H_2O has reached the thermodynamic equilibrium increasing the gas volume fraction to $\approx 33\%$ (Figure 12) and the bubble size increased from 1 cm to about 4 cm (not shown in the Figure). This time is consistent with the time scale that characterizes diffusive mass transfer of H_2O (diffusion coefficient $D = 10^{-9}$ m^2/s, Baker et al., 2005) around a bubble with radius $R \approx 2$ cm ($\tau_d = R^2/D$; Lensky et al., 2004). The

370   dissolved CO_2 is still out of thermodynamic equilibrium, as expected, because the diffusion coefficient is lower, being set to $D = 10^{-10}$ m^2/s (Baker et al., 2005). The density and viscosity of the liquid vary with the decreasing dissolved H_2O. The gas density decreases because of increasing H_2O and decreasing CO_2 that produce a decrease of the molar mass of the gas mixture.
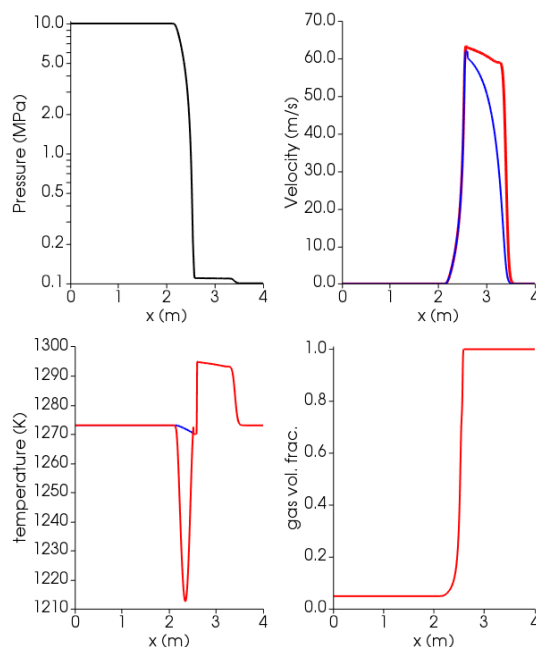
Figure 10. Results at time $t = 0.001\,\text{s}$ for the axsymmetric gas water-basalt shock tube using the Lange-Carmichael EOS (Lange and Carmichael, 1987) and the viscosity model of Giordano et al. (2008), with liquid phase switching from continuous to dispersed. Blue lines: liquid (basalt); Red lines: gas (water). At time 0, the interface dividing high pressure (left, l) from low pressure (right, r) zone is placed at 2.5 m. Initial conditions: $P_l = 10\,\text{MPa}$, $P_r = 0.1\,\text{MPa}$; $T_l = T_r = 1273\,\text{K}$ for both phases; gas volume fraction $\alpha_l = 0.05$, $\alpha_r = 1$; $U_l = U_r = 0$ for both phases. Isobaric specific heat capacities in the gas and liquid phase are, respectively, $C_{\text{P}_g} = 2510\,\text{J/kg}^{-1}\text{K}^{-1}$ (https://webbook.nist.gov/) and $C_{\text{P}_{l,\text{H}_2\text{O}}} = 2278\,\text{J/kg}^{-1}\text{K}^{-1}$, $C_{\text{P}_{l,\text{basalt}}} = 1600\,\text{J/kg}^{-1}\text{K}^{-1}$ (Lesher and Spera, 2015). Thermal conductivity of the liquid is $1.5\,\text{W}\,\text{K}^{-1}\text{m}^{-1}$ (Lesher and Spera, 2015); for the water gas phase a Prandtl number of 0.9 is used, corresponding to thermal conductivity of $0.14\,\text{W}\,\text{K}^{-1}\text{m}^{-1}$ (https://webbook.nist.gov/).

4 Conclusions

375 In this work we have presented MagmaFOAM, a library based on OpenFOAM that contains dedicated tools for the simulation of multiphase flows in magmatic systems. The MagmaFOAM implementation results in a flexible framework which is ideal for development, testing, coupling and application of the great collection of existing and future modeling strategies needed to tackle the variety of non linear multi-scale processes characterizing magma flows. MagmaFOAM includes dedicated multi-component constitutive models for dealing with realistic properties for silicate melt-gas systems as well as different utilities

380 that automatize pre- and post-processing operations. We have analyzed a number of test cases that illustrate the current capabilities and limitations of different modeling approaches in solving well-defined and reproducible flow problems, setting a solid ground for future model selection, improvement and inter-comparison studies. We have shown some of the ingredients that can be used for simulating the interaction among different silicate melts, as well as between melts and fluid phases, under different assumptions and aimed at different portions of the magmatic system (deep reservoirs vs. shallow conduits). Applica-
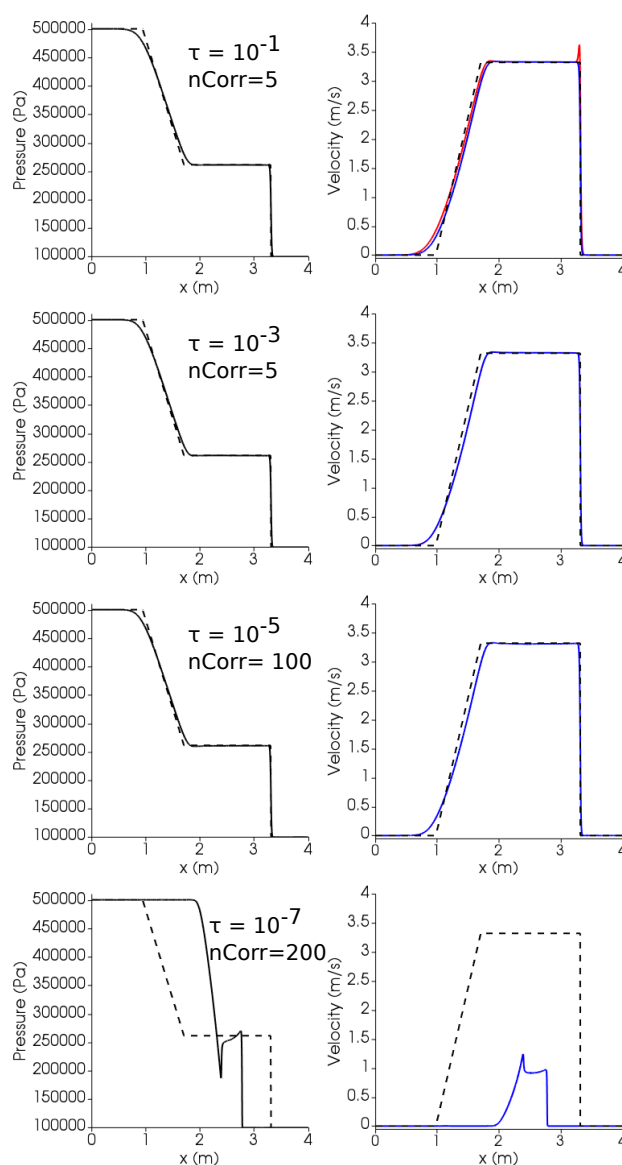
Figure 11. Air-water shock tube simulations at different relaxation times τ and number of correctors. Dashed lines: analytical solution; Solid lines: simulation. Blue lines: liquid (water); Red lines: gas (air). At time 0, the interface dividing high pressure (left, l) from low pressure (right, r) zone is placed at 2.5 m. Initial conditions: $P_l = 0.5\,\mathrm{MPa}$, $P_r = 0.1\,\mathrm{MPa}$; $T_l = T_r = 300\,\mathrm{K}$ for both phases; gas volume fraction $\alpha_l = 0.05$, $\alpha_r = 0.1$; $U_l = U_r = 0$ for both phases. Isobaric heat capacities of gas air and liquid water are, respectively, $C_{P_g} = 1004.5\,\mathrm{J/kg^{-1}K^{-1}}$ and $C_{P_l} = 4195\,\mathrm{J/kg^{-1}K^{-1}}$ (https://webbook.nist.gov/). Prandtl numbers of air and water are, respectively, 0.7 and 2.289, corresponding to thermal conductivities of $0.02\,\mathrm{W\,K^{-1}m^{-1}}$ and $0.67\,\mathrm{W\,K^{-1}m^{-1}}$, resepctively (https://webbook.nist.gov/).

Figure 12. Reacting box simulation. At time 0 a small amount of gas (volume fraction $\alpha_g = 10^{-4}$) is uniformly distributed in the box, the basaltic melt is oversaturated in H_2O (5 wt%) and CO_2 (5000 ppm) at 80 MPa and 1373 K. The diffusion coefficients for H_2O and CO_2 in the basalt are, respectively, $10^{-9}\,\mathrm{m^2/s}$ and $10^{-10}\,\mathrm{m^2/s}$ (Baker et al., 2005). Isobaric specific heat capacities in the gas and liquid phase are, respectively, $C_{P_{g,H_2O}} = 2900\,\mathrm{J/kg^{-1}K^{-1}}$, $C_{P_{g,CO_2}} = 1390\,\mathrm{J/kg^{-1}K^{-1}}$ (https://webbook.nist.gov/, Beaton et al., 1987) and $C_{P_{l,H_2O}} = 2278\,\mathrm{J/kg^{-1}K^{-1}}$, $C_{P_{l,CO_2}} = 1600\,\mathrm{J/kg^{-1}K^{-1}}$, $C_{P_{basalt}} = 1600\,\mathrm{J/kg^{-1}K^{-1}}$ (Lesher and Spera, 2015). Thermal conductivity of the liquid is $1.5\,\mathrm{W\,K^{-1}m^{-1}}$ (Lesher and Spera, 2015); for the gas phase Prandtl numbers of 0.9 for H_2O and 0.7 for CO_2 are used, corresponding to thermal conductivities of $0.16\,\mathrm{W\,K^{-1}m^{-1}}$ and $0.09\,\mathrm{W\,K^{-1}m^{-1}}$ (https://webbook.nist.gov/, Beaton et al., 1987).

385 tions of MagmaFOAM can thus include the study of magma mingling and mixing, as well as slug rising dynamics, or volatile flushing. Nevertheless, important limitations remain, most notably the development of a magma-specific mixture approach; or the intrinsic complications in modeling the transition from tight to loose phase coupling (Section 3.3.1).

The framework described in this work allows for maximum flexibility and adaptability, giving the possiblity to explore magmatic systems with different apporaches given the specific conditions aimed at. As an example, the MagmaFOAM mod-

390 ular approach allows the coupling of its bubble growth models with both single and multi-fluid solvers, Lagrangian particle tracking, or with more complex constitutive equations. Indeed, at different stages within the evolution of magmatic plumbing systems, different modeling approaches can be more appropriate to capture the fundamental physics governing the dynamics: while low-gas-fraction, deep reservoirs may well be approximated by mixture theory, at shallower levels phase decoupling becomes important and multi-fluid descriptions are more appropriate.

395 The tool is meant to be under continuous development, already underway. The addition of population balance equations to Eularian models to statistically describe the dispersed phases (bubbles and crystals) (Marchisio and Fox, 2013) will improve our understanding of how polidispersity can impact magmatic system evolution (Colucci et al., 2017a; de' Michieli Vitturi and Pardini, 2020). The inclusion of Lagrangian tracers will result in a more detailed description of the micro-physics that determines the macroscopic properties driving the dynamics. This approach in fact is more appropriate than that of Eulerian

400 models when the number of particles is too small to be treated as a continuum, or when single particles' behaviour (e.g. rapidly expanding/contracting bubbles) is so specific that they are not well represented by unique averaged fields density, velocity or temperature (e.g. Ghahramani et al., 2019). Finally, engineering applications have benefited from models that combine different approaches, e.g. interface resolving and subgrid dispersed phase modeling with single or multi fluid frameworks. These hybrid models, although not fully mature yet, allow in principle modeling at the same time the broad range of interface scales that

405 typically characterize gas-liquid flows including regime transitions (e.g., Wardle and Weller, 2013). From a volcanological perspective, predicting flow regime changes is of crucial importance to understand effusive-explosive transitions in eruptive activity (Gonnermann and Manga, 2007).

Appendix A: Linear Rayleigh Taylor instability

Figure A1b shows how a small wave number perturbation ($k = 0.15$) initially grows with slower non constant growth rate.

410 Overall this effect make the extrapolated growth rate smaller than expected. However, after a relativily small time interval, the growth rate becomes constant with a value that results to be in good agreement with the theretical one (Figure A2). This spuriuos effect gradually decreases till it diseappears as the wave number of the perturbation increases (Figure A1a). The simulations are done using the solver `interFoam` with adaptable time step ($Co_{max} = 0.01$).
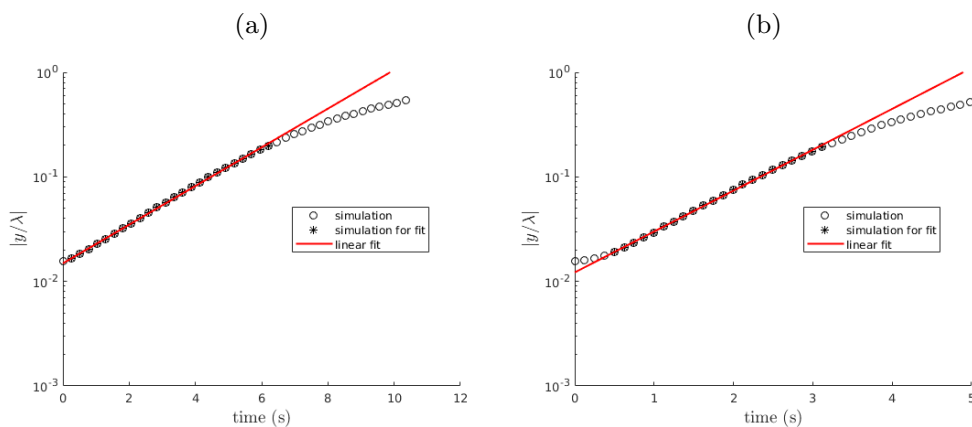
Figure A1. Time evolution of the amplitude of two single mode perturbations ($k = 0.5$ (a), and $k = 0.15$ (b)) for the linear Rayleigh Taylor instability benchmark. The growth rate of the perturbation is extrapolated with a linear regression excluding data in late (physical) and eventually early (spurious) phases characterised by non linear effects (data not marked with an asterisk).
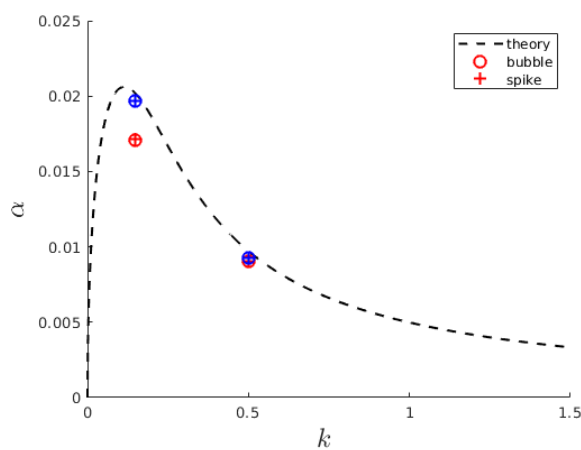
Figure A2. Extrapolated growth rate for two perturbations with linear regression excluding (blue) or not (red) data in the initial phase characterised by non linear spurious effects.

Appendix B: multiComponentODERPShellDStatic: model equations

415 A modified form of the Rayleigh-Plesset equation describes the hydrodynamics of the growth of a multi component spherical bubble in a finite incompressible shell of liquid of radius S.

$$\rho R \frac{d^2 R}{dt^2} \left(1 - \frac{R}{S}\right) + \rho \left(\frac{dR}{dt}\right)^2 \left(\frac{3}{2} - \frac{2R}{S} + \frac{R^4}{2S^4}\right) = \tag{B1}$$

$$p_G(t) - p_l(t) + 4\frac{dR}{dt}R^2 \left(-3 \int_R^S \frac{\mu(r)}{r^4} dr\right) - \frac{2\sigma}{R}.$$

In the above, ρ_l is the liquid density, R is the bubble radius, S is the radius of the shell ($S^3 = S_0^3 + R^3(t)$), p_G is the gas
420 pressure inside the bubble, p_l is the pressure acting on the outside of the liquid shell, σ is the surface tension, t is the time and μ is the liquid dynamic viscosity that depends on the concentration of dissolved volatiles in the shell. Given $p_l(t)$ this represents an equation that can be solved to find $R(t)$ provided $p_G(t)$. p_G is given by combining the mass conservation of the gas phase with an equation of state for a perfect gas. Mass conservation of the gas phase is given by

$$\frac{d}{dt}\left(R^3 \rho_G\right) = 3R^2 \rho_l \sum_{i=1}^{N} D_i \left[\frac{\partial C_i}{\partial r}\right]_{r=R}, \tag{B2}$$

425 where D_i is the mass diffusivity and C_i the concentration of the i-th species dissolved in the melt. Mass conservation of the i-th dissolved specie is given by

$$\frac{d}{dt}\left(R^3 \rho_G Y_i\right) = 3R^2 \rho_l D_i \left[\frac{\partial C_i}{\partial r}\right]_{r=R}, \tag{B3}$$

where Y_i is the concentration in the gas phase. Assuming local thermodynamic equilibrium at the bubble-melt interface (i.e., $C_i(R) = C_{i,\mathrm{sat}}(p_G)$), a zero gradient boundary conditions at the shell boundary and a quasi-static diffusion in the shell
430 (Lyakhovsky et al., 1996), the term in square brackets in equations (B2) and (B3) is given by

$$\left[\frac{dC_i}{dr}\right]_{r=R} = \frac{S_0^3 \left(C_{i,0} - C_{i,sat}\right) + \frac{1}{\rho_l}\left(R_0^3 \rho_{g,0} Y_{i,0} - R^3 \rho_g Y_i\right)}{S_0^3 R - \frac{3}{2}\left(S^2 - R^2\right)R^2}. \tag{B4}$$

Assuming constant viscosity, the term in eq. (B1) is analytically integrated to obtain

$$\left(-3 \int_R^S \frac{\mu(C_i(r))}{r^4} dr\right) = \mu \left(\frac{1}{S^3} - \frac{1}{R^3}\right). \tag{B5}$$

For a monodispersed distribution, the gas volume fraction is given by

435 $$\alpha = \frac{R^3}{S^3}. \tag{B6}$$

Appendix C: Shock Tube

Figures C1, C2 and C3 show results from the single phase shock tube simulations discussed in Section 3.3.1. Figure C4 shows results from the air-water shock-tube with liquid phase switching from conituous to dispersed.
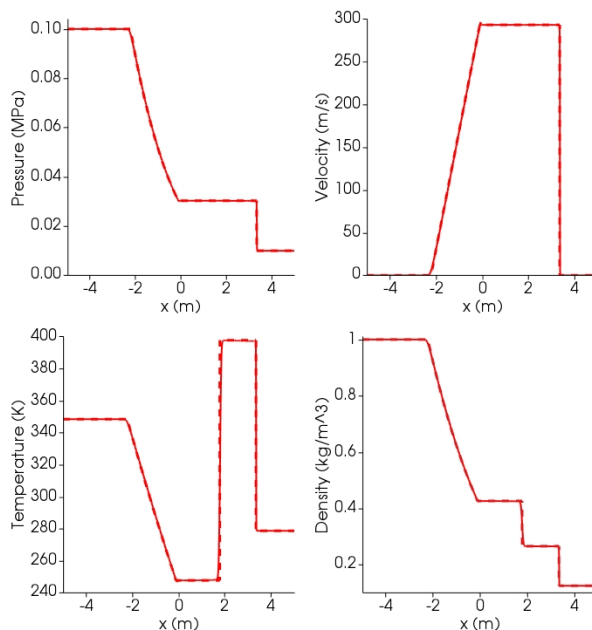
Figure C1. Results at time $t = 0.006\,\mathrm{s}$ for the air Sod shock tube. Dashed lines: analytical solution; Solid lines: simulation. At time 0, the interface dividing high pressure (left, l) from low pressure (right, r) zone is placed at 0 m. Initial conditions: $P_l = 0.1\,\mathrm{MPa}$, $P_r = 0.01\,\mathrm{MPa}$; $T_l = 348.432\,\mathrm{K}$, $T_r = 278.746\,\mathrm{K}$; gas volume fraction $\alpha_l = 1$, $\alpha_r = 0$; $U_l = U_r = 0$. Isobaric heat capacity is $C_P = 1004.5\,\mathrm{J\,kg^{-1}K^{-1}}$, corresponding to heat capacity ratio $\gamma = 1.4$.

Appendix D: Magmatic Compositions

440 Table D1 reports the compositions in terms of major oxides of the magmas used in the simulations shown in the manuscript.
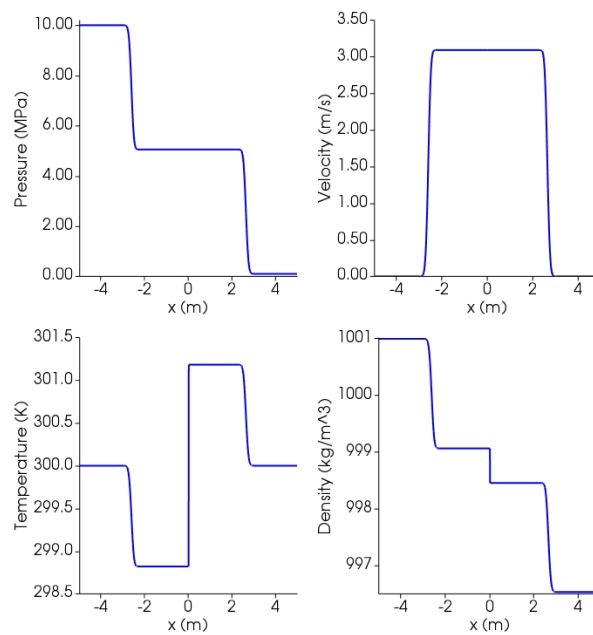
Figure C2. Results at time $t = 0.00164$ s for single-phase shock tube with liquid water using SPWAT EOS. At time 0, the interface dividing high pressure (left, l) from low pressure (right, r) zone is placed at 0. Initial conditions: $P_l = 10$ MPa, $P_r = 0.1$ MPa; $T_l = T_r = 300$ K; gas volume fraction $\alpha_l = \alpha_r = 0$; $U_l = U_r = 0$. Isobaric heat capacity is $C_P = 4195$ J kg^{-1}K^{-1} (https://webbook.nist.gov/).
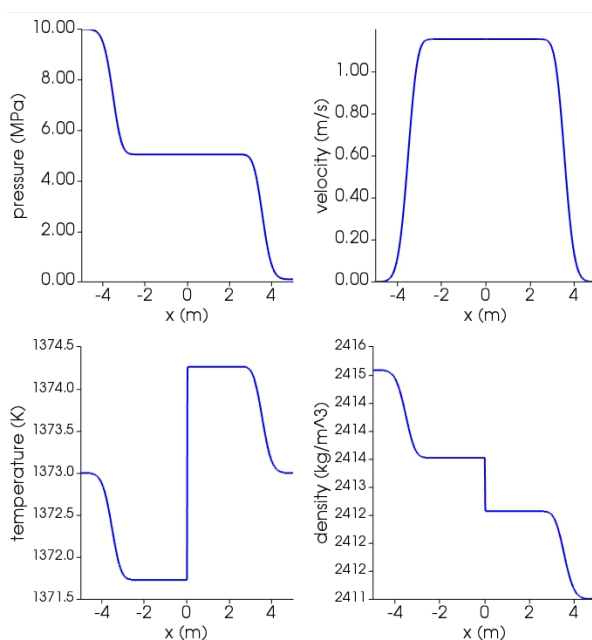
Figure C3. Results at time $t = 0.002\,\mathrm{s}$ for single-phase shock tube with basaltic melt using Lange-Carmichael EOS. At time 0, the interface dividing high pressure (left, l) from low pressure (right, r) zone is placed at 0. Initial conditions: $P_\mathrm{l} = 10\,\mathrm{MPa}$, $P_\mathrm{r} = 0.1\,[MPa$; $T_\mathrm{l} = T_\mathrm{r} = 1373\,\mathrm{K}$; gas volume fraction $\alpha_\mathrm{l} = \alpha_\mathrm{r} = 0$; $U_\mathrm{l} = U_\mathrm{r} = 0$. Isobaric heat capacity is $C_\mathrm{P} = 1600\,\mathrm{J\,kg^{-1}K^{-1}}$ (Lesher and Spera, 2015). Thermal conductivity is $1.5\,\mathrm{W\,K^{-1}m^{-1}}$ (Lesher and Spera, 2015).
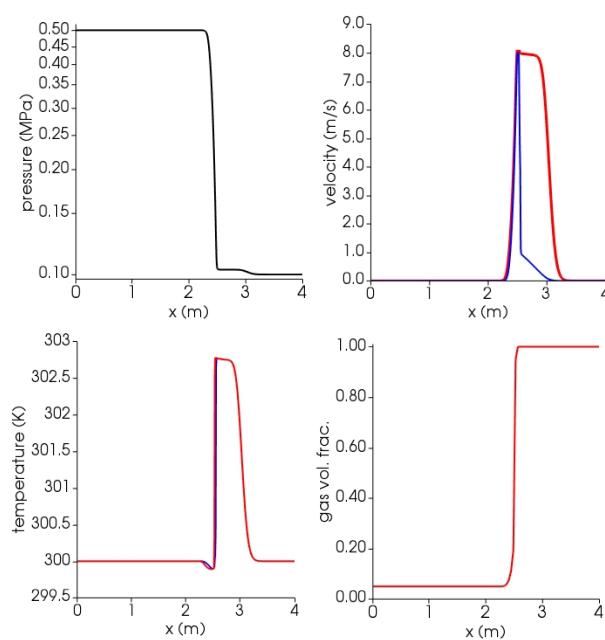
Figure C4. Results at time $t = 0.0015\,\mathrm{s}$ for the air-water shock tube with liquid phase switching from continuous to dispersed. Blue lines: liquid (water); Red lines: gas (air). At time 0, the interface dividing high pressure (left, l) from low pressure (right, r) zone is placed at 2.5 m. Initial conditions: $P_\mathrm{l} = 0.5\,\mathrm{MPa}$, $P_\mathrm{r} = 0.1\,\mathrm{MPa}$; $T_\mathrm{l} = T_\mathrm{r} = 300\,\mathrm{K}$ for both phases; gas volume fraction $\alpha_\mathrm{l} = 0.05$, $\alpha_\mathrm{r} = 1$; $U_\mathrm{l} = U_\mathrm{r} = 0$ for both phases. Isobaric heat capacities of gas air and liquid water are, respectively, $C_{\mathrm{P}_\mathrm{g}} = 1004.5\,\mathrm{J\,kg^{-1}K^{-1}}$ and $C_{\mathrm{P}_\mathrm{l}} = 4195\,\mathrm{J\,kg^{-1}K^{-1}}$ (https://webbook.nist.gov/). Prandtl numbers of air and water are, respectively, 0.7 and 2.289, corresponding to thermal conductivities of $0.02\,\mathrm{W\,K^{-1}m^{-1}}$ and $0.67\,\mathrm{W\,K^{-1}m^{-1}}$ (https://webbook.nist.gov/).

Table D1. Oxides composition for the magmas used in benchmarking simulations. Amounts are relative.

	SiO_2	TiO_2	AlO_2	Fe_2O_3	FeO	MnO	MgO	CaO	Na_2O	K_2O
andesite	0.587	0.0088	0.1724	0.0331	0.0409	0.0014	0.0337	0.0688	0.0353	0.0164
basalt	0.484	0.0167	0.178	0.0186	0.0836	0.0018	0.0553	0.102	0.0387	0.0211

Code and data availability. The version of the model used to produce the results shown in this paper, as well as input data and scripts to replicate all the simulations presented in this paper, are archived on Zenodo (Brogi et al., 2021).

Author contributions. FB and SC developed and tested the software, including pre- and post-processing, performed the simulations and wrote the first draft of the paper. CPM contributed to paper writing and supervised the work. JM worked on bubble dynamics and its analysis.
445 MdMV provided guidance and help on the multifluid solver. PP provided supervision and reviewed the original draft.

Competing interests. The Authors declare no competing interests.

Acknowledgements. This work has been supported by Istituto Nazionale di Geofisica e Vulcanologia (INGV) and Istituto Nazionale di Oceanografia e Geofisica Sperimentale (OGS) under HPC-TRES program award no 2016-05 to F. Brogi. This research has received funding from European Union's Horizon 2020 research and innovation programme under the EUROVOLC project, grant agreement no 731070, and
450 under the ChEESE project, grant agreement no 823844; and from Italy's MIUR PRIN grant 2015L33WAK.

References

Bachmann, O. and Bergantz, G. W.: Rejuvenation of the Fish Canyon magma body: A window into the evolution of large-volume silicic magma systems, Geology, 31, 789–792, 2003.

Bagagli, M., Montagna, C. P., Papale, P., and Longo, A.: Signature of magmatic processes in strainmeter records at Campi Flegrei (Italy), Geophys. Res. Lett., 44, 718–725, https://doi.org/10.1002/2016GL071875, 2017.

Baker, D. R., Freda, C., Brooker, R. A., and Scarlato, P.: Volatile diffusion in silicate melts and its effects on melt inclusions, ANNALS OF GEOPHYSICS, 48, 699 – 717, 2005.

Beaton, C., Edwards, D., and Schlünder, E.: Heat Exchanger Design Handbook: HEDH.. Physical properties, v. 5, VDI-Verlag, 1987.

Bergantz, G., Schleicher, J., and Burgisser, A.: Open-system dynamics and mixing in magma mushes, Nature Geoscience, 8, 793, 2015.

Brogi, F., Colucci, S., and Montagna, C. P.: MagmaFOAM-1.0: a modular framework for the simulation of magmatic systems, https://doi.org/10.5281/zenodo.5031825, a public gitLab repository will be soon available, 2021.

Burgisser, A., Alletti, M., and Scaillet, B.: Simulating the behavior of volatiles belonging to the C–O–H–S system in silicate melts under magmatic conditions with the software D-Compress, Computers & Geosciences, 79, 1–14, 2015.

Burnham, C. W. and Davis, N.: The role of H2O in silicate melts; II, Thermodynamic and phase relations in the system NaAlSi3O8-H2O to 10 kilobars, 700 degrees to 1100 degrees C, American Journal of Science, 274, 902–940, 1974.

Cerminara, M., Esposti Ongaro, T., and Berselli, L. C.: ASHEE-1.0: a compressible, equilibrium–Eulerian model for volcanic ash plumes, Geoscientific Model Development, 9, 697–730, 2016.

Chandrasekhar, S.: The character of the equilibrium of an incompressible heavy viscous fluid of variable density, in: Mathematical Proceedings of the Cambridge Philosophical Society, vol. 51, pp. 162–178, Cambridge University Press, 1955.

Chandrasekhar, S.: Hydrodynamic and hydromagnetic stability, Courier Corporation, 2013.

Chouet, B., Dawson, P., and Nakano, M.: Dynamics of diffusive bubble growth and pressure recovery in a bubbly rhyolitic melt embedded in an elastic solid, Journal of Geophysical Research: Solid Earth, 111, https://doi.org/10.1029/2005JB004174, 2006.

Colucci, S., Battaglia, M., and Trigila, R.: A thermodynamical model for the surface tension of silicate melts in contact with H_2O gas, Geochimica et Cosmochimica Acta, 175, 127, https://doi.org/10.1016/j.gca.2015.10.037, 2016.

Colucci, S., de' Michieli Vitturi, M., and Landi, P.: CrystalMom: a new model for the evolution of crystal size distributions in magmas with the quadrature-based method of moments, Contrib. Mineral. Petrol., 172:100, https://doi.org/10.1007/s00410-017-1421-6, 2017a.

Colucci, S., Papale, P., and Montagna, C. P.: Non-Newtonian flow of bubbly magma in volcanic conduits, J. Geophys. Res. Solid Earth, pp. 1–16, https://doi.org/10.1002/2016JB013383, 2017b.

Costa, A., Suzuki, Y. J., Cerminara, M., Devenish, B. J., Ongaro, T. E., Herzog, M., Van Eaton, A. R., Denby, L., Bursik, M., de' Michieli Vitturi, M., et al.: Results of the eruptive column model inter-comparison study, Journal of Volcanology and Geothermal Research, 326, 2–25, 2016.

Coumans, J., Llewellin, E., Wadsworth, F., Humphreys, M., Mathias, S., Yelverton, B., and Gardner, J.: An experimentally validated numerical model for bubble growth in magma, Journal of Volcanology and Geothermal Research, 402, 107 002, https://doi.org/10.1016/j.jvolgeores.2020.107002, 2020.

Cussler, E. L.: Diffusion mass transfer in fluid systems, 2009.

de' Michieli Vitturi, M. and Pardini, F.: PLUME-MoM-TSM 1.0.0: A volcanic columns and umbrella cloud spreading model, Geoscientific Model Development Discussions, 2020, 1–46, https://doi.org/10.5194/gmd-2020-227, 2020.

de' Michieli Vitturi, M., Clarke, A., Neri, A., and Voight, B.: Effects of conduit geometry on magma ascent dynamics in dome-forming eruptions, Earth and Planetary Science Letters, 272, 567–578, 2008a.

490 de' Michieli Vitturi, M., Clarke, A., Neri, A., and Voight, B.: Effects of conduit geometry on magma ascent dynamics in dome-forming eruptions, Earth and Planetary Science Letters, 272, 567–578, https://doi.org/10.1016/j.epsl.2008.05.025, 2008b.

de' Michieli Vitturi, M., Neri, A., and Barsotti, S.: PLUME-MoM 1.0: A new integral model of volcanic plumes based on the method of moments, Geoscientific Model Development, 8, 2447–2463, https://doi.org/10.5194/gmd-8-2447-2015, 2015.

Deshpande, S. S., Anumolu, L., and Trujillo, M. F.: Evaluating the performance of the two-phase flow solver interFoam, Computational
495 science & discovery, 5, 014 016, 2012.

Druitt, T. H., Costa, F., Deloule, E., Dungan, M., and Scaillet, B.: Decadal to monthly timescales of magma transfer and reservoir growth at a caldera volcano, Nature, 482, 77–80, https://doi.org/10.1038/nature10706, 2012.

Dufek, J.: The Fluid Mechanics of Pyroclastic Density Currents, Annual Review of Fluid Mechanics, 48, 459–485, https://doi.org/10.1146/annurev-fluid-122414-034252, 2016.

500 Dufek, J. and Bergantz, G.: Transient two-dimensional dynamics in the upper conduit of a rhyolitic eruption: A comparison of closure models for the granular stress, Journal of Volcanology and Geothermal Research, 143, 113–132, 2005.

Duff, R., Harlow, F., and Hirt, C.: Effects of diffusion on interface instability between gases, The Physics of Fluids, 5, 417–425, 1962.

Esposti Ongaro, T., Cavazzoni, C., Erbacci, G., Neri, A., and Salvetti, M.: A parallel multiphase flow code for the 3D simulation of explosive volcanic eruptions, Parallel Computing, 33, 541–560, https://doi.org/10.1016/j.parco.2007.04.003, 2007.

505 Garg, D., Papale, P., Colucci, S., and Longo, A.: Long-lived compositional heterogeneities in magma chambers, and implications for volcanic hazard, Scientific reports, 9, 3321, 2019.

Ghahramani, E., Arabnejad, M. H., and Bensow, R. E.: A comparative study between numerical methods in simulation of cavitating bubbles, International Journal of Multiphase Flow, 111, 339 – 359, https://doi.org/10.1016/j.ijmultiphaseflow.2018.10.010, 2019.

Giordano, D., Russell, J. K., and Dingwell, D. B.: Viscosity of magmatic liquids: a model, Earth and Planetary Science Letters, 271, 123–134,
510 2008.

Gonnermann, H. M. and Manga, M.: The Fluid Mechanics Inside a Volcano, Annu. Rev. Fluid Mech., 39, 321–356, https://doi.org/10.1146/annurev.fluid.39.050905.110207, 2007.

Grace, J.: Shapes and velocities of bubbles rising in infinite liquid, Transactions of the Institution of Chemical Engineers, 51, 116–120, 1973.

Griffiths, R. W.: The Dynamics of Lava Flows, Annual Review of Fluid Mechanics, 32, 477–518,
515 https://doi.org/10.1146/annurev.fluid.32.1.477, 2000.

He, X., Chen, S., and Zhang, R.: A lattice Boltzmann scheme for incompressible multiphase flow and its application in simulation of Rayleigh–Taylor instability, Journal of Computational Physics, 152, 642–663, 1999.

Huber, C., Su, Y., Nguyen, C., Parmigiani, A., Gonnermann, H. M., and Dufek, J.: A new bubble dynamics model to study bubble growth, deformation, and coalescence, Journal of Geophysical Research: Solid Earth, 119, 216–239, 2014.

520 Ishi, M. and Hibiki, T.: Thermo-fluid dynamics of two-phase flow, 2006.

Issa, R. I.: Solution of the implicitly discretised fluid flow equations by operator-splitting, Journal of computational physics, 62, 40–65, 1986.

Jackson, M. D., Blundy, J. D., and Sparks, R. S. J.: Chemical differentiation, cold storage and remobilization of magma in the Earth's crust, Nature, 564, 405–409, https://doi.org/10.1038/s41586-018-0746-2, 2018.

Jellinek, a. M., Kerr, R. C., and Griffiths, R. W.: Mixing and compositional stratification produced by natural convection: 1. Experiments and
525 their application to Earth's core and mantle, Journal of Geophysical Research, 104, 7183, https://doi.org/10.1029/1998JB900116, 1999.

Karema, H. and Lo, S.: Efficiency of interphase coupling algorithms in fluidized bed conditions, Computers & Fluids, 28, 323 – 360, https://doi.org/10.1016/S0045-7930(98)00028-0, 1999.

Keller, T. and Suckale, J.: A continuum model of multi-phase reactive transport in igneous systems, Geophysical Journal International, 219, 185–222, https://doi.org/10.1093/gji/ggz287, 2019.

530   Koyaguchi, T. and Mitani, N. K.: A theoretical model for fragmentation of viscous bubbly magmas in shock tubes, Journal of Geophysical Research: Solid Earth, 110, 2005.

La Spina, G., de' Michieli Vitturi, M., and Clarke, A.: Transient numerical model of magma ascent dynamics: application to the explosive eruptions at the Soufrière Hills Volcano, Journal of Volcanology and Geothermal Research, 336, 118–139, 2017.

Lange, R. A. and Carmichael, I. S.: Densities of Na2O-K2O-CaO-MgO-FeO-Fe2O3-Al2O3-TiO2-SiO2 liquids: new measurements and

535   derived partial molar properties, Geochimica et Cosmochimica Acta, 51, 2931–2946, 1987.

Lensky, N. G., Lyakhovsky, V., and Navon, O.: Radial variations of melt viscosity around growing bubbles and gas overpressure in vesiculating magmas, Earth and Planetary Science Letters, 186, 1–6, 2001.

Lensky, N. G., , Navon, O., and Lyakhovsky, V.: Bubble growth during decompression of magma: experimental and theoretical investigation, Journal of Volcanology and Geothermal Research, 129, 7–22, 2004.

540   Lesher, C. E. and Spera, F. J.: Thermodynamic and transport properties of silicate melts and magma, in: The Encyclopedia of Volcanoes (Second Edition), pp. 113–141, Elsevier, 2015.

Longo, A., Papale, P., Vassalli, M., Saccorotti, G., Montagna, C. P., Cassioli, A., Giudice, S., and Boschi, E.: Magma convection and mixing dynamics as a source of ultra-long-period oscillations, Bulletin of Volcanology, 74, 873–880, 2012.

Lyakhovsky, V., Hurwitz, S., and Navon, O.: Bubble growth in rhyolitic melts: experimental and numerical investigation, Bull. Volcanol., 58,

545   19–32, https://doi.org/10.1007/s004450050122, 1996.

Macedonio, G., Neri, A., Martì, J., and Folch, A.: Temporal evolution of flow conditions in sustained magmatic explosive eruptions, Journal of Volcanology and Geothermal Research, 143, 153–172, https://doi.org/10.1016/j.jvolgeores.2004.09.015, 2005.

Marchisio, D. L. and Fox, R. O.: Multiphase reacting flows: modelling and simulation, Springer, 2007.

Marchisio, D. L. and Fox, R. O.: Computational Models for Polydisperse Particulate and Multiphase Systems, Cambridge Series in Chemical

550   Engineering, Cambridge University Press, https://doi.org/10.1017/CBO9781139016599, 2013.

Martí, J., Zafrilla, S., Andújar, J., Jiménez-Mejías, M., Scaillet, B., Pedrazzi, D., Doronzo, D., and Scaillet, S.: Controls of magma chamber zonation on eruption dynamics and deposits stratigraphy: The case of El Palomar fallout succession (Tenerife, Canary Islands), Journal of Volcanology and Geothermal Research, 399, 106 908, https://doi.org/10.1016/j.jvolgeores.2020.106908, 2020.

Massol, H. and Koyaguchi, T.: The effect of magma flow on nucleation of gas bubbles in a volcanic conduit, Journal of Volcanology and

555   Geothermal Research, 143, 69–88, https://doi.org/10.1016/j.jvolgeores.2004.09.011, 2005.

Melnik, O.: Dynamics of two-phase conduit flow of high-viscosity gas-saturated magma: large variations of sustained explosive eruption intensity, Bulletin of Volcanology volume, 62, 153–170, https://doi.org/10.1007/s004450000072, 2000.

Melnik, O. and Sparks, S.: Transient models of conduit flows during volcanic eruptions, Statistics in Volcanology, pp. 201–214, 2006.

Mitchner, M. and Landshoff, R.: Rayleigh-Taylor Instability for Compressible Fluids, The Physics of Fluids, 7, 862–866, 1964.

560   Moin, P. and Mahesh, K.: Direct numerical simulation: a tool in turbulence research, Annual review of fluid mechanics, 30, 539–578, 1998.

Montagna, C., Papale, P., and Longo, A.: Timescales of mingling in shallow magmatic reservoirs, Geological Society, London, Special Publications, 422, SP422–6, 2015.

Morgavi, D., Arienzo, I., Montagna, C. P., Perugini, D., and Dingwell, D. B.: Magma Mixing: History and Dynamics of an Eruption Trigger, in: Volcanic Unrest, pp. 123–137, https://doi.org/10.1007/11157_2017_30, 2017.

565 Neri, A., Esposti Ongaro, T., Macedonio, G., and Gidaspow, D.: Multiparticle simulation of collapsing volcanic columns and pyroclastic flow, Journal of Geophysical Research: Solid Earth, 108, 2003.

Newman, S. and Lowenstern, J. B.: VolatileCalc: a silicate melt–H2O–CO2 solution model written in Visual Basic for excel, Computers & Geosciences, 28, 597–604, https://doi.org/https://doi.org/10.1016/S0098-3004(01)00081-4, 2002.

Ongaro, T. E., Cavazzoni, C., Erbacci, G., Neri, A., and Salvetti, M.-V.: A parallel multiphase flow code for the 3D simulation of explosive
570 volcanic eruptions, Parallel Computing, 33, 541–560, 2007.

Papale, P.: Modeling of the solubility of a two-component H2O+ CO2 fluid in silicate liquids, American Mineralogist, 84, 477–492, 1999.

Papale, P.: Dynamics of magma flow in volcanic conduits with variable fragmentation efficiency and nonequilibrium pumice degassing, J. Geophys. Res., 106, 11 043, https://doi.org/10.1029/2000JB900428, 2001.

Papale, P., Moretti, R., and D., B.: The compositional dependence of the saturation surface of $H_2O + CO_2$ fluids in silicate melts, Chemical
575 Geology, 229, 78–95, 2006.

Parmigiani, A., Huber, C., and Bachmann, O.: Mush microphysics and the reactivation of crystal-rich magma reservoirs, Journal of Geophysical Research: Solid Earth, 119, 6308–6322, 2014.

Perugini, D. and Poli, G.: The mixing of magmas in plutonic and volcanic environments: Analogies and differences, Lithos, 153, 261–277, https://doi.org/10.1016/j.lithos.2012.02.002, 2012.

580 Perugini, D., Poli, G., Petrelli, M., De Campos, C., and Dingwell, D.: Time-scales of recent Phlegrean Fields eruptions inferred from the application of a 'diffusive fractionation' model of trace elements, Bulletin of Volcanology, 72, 431–447, https://doi.org/10.1007/s00445-009-0329-z, 2010.

Proussevitch, A. A. and Sahagian, D. L.: Dynamics and energetics of bubble growth in magmas: Analytical formulation and numerical modeling, Journal of Geophysical Research, 103, 18,223–18,251, 1998.

585 Proussevitch, A. A., Sahagian, D. L., and Anderson, A. T.: Dynamics of Diffusive Bubble Growth in Magmas: Isothermal Case, Journal of Geophysical Research, 98, 22,283–22,307, 1993.

Roenby, J., Larsen, B. E., Bredmose, H., and Jasak, H.: A new volume-of-fluid method in openfoam, in: VII International Conference on Computational Methods in Marine Engineering. Nantes: International Center for Numerical Methods in Engineering, 2017.

Ruprecht, P., Bergantz, G. W., and Dufek, J.: Modeling of gas-driven magmatic overturn: Tracking of phenocryst dispersal and gathering
590 during magma mixing, Geochemistry, Geophysics, Geosystems, 9, 2008.

Sahagian, D. and Proussevitch, A.: Standardized model runs and sensitivity analysis using the "Bubbledrive-1" volcanic conduit flow model, Journal of Volcanology and Geothermal Research, 143, 173–185, https://doi.org/10.1016/j.jvolgeores.2004.09.016, 2005.

Samkhaniani, N., Ajami, A., Kayhani, M. H., and Dari, A. S.: Direct numerical simulation of single bubble rising in viscous stagnant liquid, in: International Conference on Merchanical, Automobile and Robotics Engineering, 2012.

595 Scopigno, T., Ruocco, G., Sette, F., and Monaco, G.: Is the fragility of a liquid embedded in the properties of its glass?, Science, 302, 849–852, 2003.

Seropian, G., Rust, A. C., and Sparks, R. S. J.: The gravitational stability of lenses in magma mushes: confined Rayleigh-Taylor instabilities, J. Geophys. Res. Solid Earth, https://doi.org/10.1029/2018JB015523, 2018.

Shimomura, Y., Nishimura, T., and Sato, H.: Bubble growth processes in magma surrounded by an elastic medium, Journal of Volcanology
600 and Geothermal Research, 155, 307 – 322, https://doi.org/10.1016/j.jvolgeores.2006.04.003, 2006.

Sparks, R. S. J.: Forecasting volcanic eruptions, Earth and Planetary Science Letters, 210, 1–15, https://doi.org/10.1016/S0012-821X(03)00124-9, 2003.

Stadtke, H.: Gasdynamic Aspects of Two-Phase Flow, 2006.

Suckale, J., Hager, B. H., Elkins-Tanton, L. T., and Nave, J.-C.: It takes three to tango: 2. Bubble dynamics in basaltic volcanoes and
605   ramifications for modeling normal Strombolian activity, Journal of Geophysical Research: Solid Earth, 115, 2010a.

Suckale, J., Nave, J.-C., and Hager, B. H.: It takes three to tango: 1. Simulating buoyancy-driven flow in the presence of large viscosity
        contrasts, Journal of Geophysical Research: Solid Earth, 115, 2010b.

Suzuki, Y. J., Koyaguchi, T., Ogawa, M., and Hachisu, I.: A numerical study of turbulent mixing in eruption clouds using a three-dimensional
        fluid dynamics model, Journal of Geophysical Research: Solid Earth, 110, 2005.

610 Venier, C. M., Marquez Damian, S., and Nigro, N. M.: Numerical aspects of Eulerian gas–particles flow formulations, Computers & Fluids,
        133, 151 – 169, https://doi.org/10.1016/j.compfluid.2016.05.003, 2016.

Wardle, K. E. and Weller, H. G.: Hybrid multiphase CFD solver for coupled dispersed/segregated flows in liquid-liquid extraction, Interna-
        tional Journal of Chemical Engineering, 2013, 2013.

Wark, D., Hildreth, W., Spear, F., Cherniak, D., and Watson, E.: Pre-eruption recharge of the Bishop magma system, Geology, 35, 235,
615   https://doi.org/10.1130/G23316A.1, 2007.

Winden, B.: An Open-Source Framework for Ship Performance CFD, in: SNAME 26th Offshore Symposium, OnePetro, 2021.

Xie, C., Tao, J., and Li, J.: Viscous Rayleigh-Taylor instability with and without diffusion effect, Applied Mathematics and Mechanics, 38,
        263–270, 2017.